

Article

Preparation of Porous Activated Carbons for High Performance Supercapacitors from Taixi Anthracite by Multi-Stage Activation

Xiao-Ming Yue ^{1,*}, Zhao-Yang An ¹, Mei Ye ¹, Zi-Jing Liu ¹, Cui-Cui Xiao ¹, Yong Huang ², Yu-Jia Han ¹, Shuang-Quan Zhang ^{1,*} and Jun-Sheng Zhu ¹

¹ Key Laboratory of Coal Processing and Efficient Utilization (Ministry of Education) and School of Chemical Engineering and Technology, China University of Mining and Technology, Xuzhou 221116, China; azy15050837569@163.com (Z.-Y.A.); ye19851623526@163.com (M.Y.); zj18361272159@163.com (Z.-J.L.); 19851625722@163.com (C.-C.X.); 18361227609@163.com (Y.-J.H.); zhujschina@163.com (J.-S.Z.)

² College of Materials Science and Engineering, Nanjing Forestry University, Nanjing 210037, China; huangyong@njfu.edu.cn

* Correspondence: yuexiaoming_cumt@126.com (X.-M.Y.); cumtzsq@126.com (S.-Q.Z.); Tel.: +86-137-7598-7409 (X.-M.Y.); +86-135-1256-7750 (S.-Q.Z.)

Received: 9 September 2019; Accepted: 3 October 2019; Published: 5 October 2019



Abstract: Coal-based porous materials for supercapacitors were successfully prepared using Taixi anthracite (TXA) by multi-stage activation. The characterization and electrochemical tests of activated carbons (ACs) prepared in different stages demonstrated that the AC from the third-stage activation (AC_{III}) shows good porous structures and excellent electrochemical performances. AC_{III} exhibited a fine specific capacitance of 199 F g⁻¹ at a current density of 1 A g⁻¹ in the three-electrode system, with 6 mol L⁻¹ KOH as the electrolyte. The specific capacitance of AC_{III} remained 190 F g⁻¹ even despite increasing the current density to 5 A g⁻¹, indicating a good rate of electrochemical performance. Moreover, its specific capacitance remained at 98.1% of the initial value after 5000 galvanostatic charge-discharge (GCD) cycle tests at a current density of 1 A g⁻¹, suggesting that the AC_{III} has excellent cycle performance as electrode materials for supercapacitors. This study provides a promising approach for fabricating high performance electrode materials from high-rank coals, which could facilitate efficient and clean utilization of high-rank coals.

Keywords: supercapacitor; multi-stage activation; coal-based electrodes; activated carbon; electrochemical performance

1. Introduction

With the depletion of fossil energy, the storage and conversion of renewable energy has become an urgent problem in the world today [1]. As a kind of high-efficiency energy storage device, supercapacitors have attracted people's attention due to their characteristics of fast charge-discharge rate, high coulombic efficiency, excellent rate performance, and long cycle life [2–5]. Electrode materials are the key factors determining the performance of supercapacitors. At present, they are mainly divided into three categories: carbon materials, transition metal oxides, and conductive polymers [6,7]. Carbon materials mainly include activated carbon (AC) [8,9], carbon fiber [10,11], carbon nanotubes [12,13], carbon nanosheets [14,15], graphene [16–18], etc.

There are abundant coal resources in China, and coal will remain a major source of energy for quite a long time in China. It is very significant and meaningful to research how to use coal efficiently and cleanly, and convert cheap coal into usable materials. As is well-known, coal has become the most commonly used precursor for production of AC because of its abundant resources, low cost, and high

carbon content [19], and coal-based porous carbon has been widely researched for supercapacitor electrodes. Dong et al. [20] reported interconnected porous carbon nanosheet/nickel foam composites which were obtained from coal tar pitch coupled with KOH activation. Qin et al. [21] synthesized the interconnected porous carbons from coal tar pitch and microcrystalline cellulose for high-performance supercapacitors. Wang et al. [22] reported a porous carbon with the $1851 \text{ m}^2 \text{ g}^{-1}$ specific surface area prepared from Xinjiang anthracite through chemical activation with ZnCl_2 , where the specific capacitance reaches 178 F g^{-1} at 1 A g^{-1} . The chemical activators such as KOH were usually added to coal in solid state to prepare coal-based electrode materials in most papers [23,24]. Although this method could produce large surface areas AC, it led to a large amount of activator (activator and coal with mass ratios of 3:1 to 5:1, commonly) and serious corrosion of equipment because the utilization of activator is low, more importantly, the surface areas of the AC has not been effectively utilized through the energy storage process. Therefore, it is necessary to find a low-cost, simple, and environmentally friendly method to produce high-performance supercapacitors. In this work, impregnation method was used to prepare AC with Taixi anthracite (TXA) as a precursor. First, the columnar coal strips were carbonized and physical activated with CO_2 , then chemically activated after immersion with KOH solution, next, re-impregnated with KOH solution, and activated again. CO_2 activation can make the material have a certain pore structure, which is beneficial to improving the effect of the impregnation method. It is found that the electrochemical performance of the ACs can be effectively improved by increasing the number of impregnation and activation processes. In addition, it is worth noting that the mass ratio of the activator (KOH) to carbon is only about 1:3 in both chemical activations that followed. The method of impregnation can reduce the KOH application amount so that the risk of corrosion of equipment can be reduced too, and the remaining KOH can be recycled.

2. Results and Discussion

2.1. Microstructure and Composition

The SEM images of TXA and the ACs obtained in each stage are shown in Figure 1. As shown in Figure 1a, TXA has a dense surface and almost no obvious pores, which is attributed to the high degree of coalification of anthracite, which has relatively low porosity. As illustrated in Figure 1b, after the first stage of physical activation, some observable pores appear on the surface of the AC_I and there are some irregular fragments on the surface and in the crack of the AC_I . As Figure 1c shows, after the second stage of chemical activation, more pores (the large pores we can see on the SEM image) appear on the surface of the AC_{II} than AC_I . This means the number of macropores of the AC_{II} is increased, which can shorten the distance of electrolyte ions diffusing into the micropores in supercapacitor, thereby improving the electrochemical properties of electrode material [25,26]. Irregular fragments of AC_{II} are reduced due to washing with HCl solution and deionized water. AC_{II} was used as the raw material to repeat the impregnation with the KOH activator and activation process to obtain AC_{III} . As illustrated in Figure 1d, compared with the SEM images of TXA, AC_I , and AC_{II} , the surface of AC_{III} is more abundantly porous, and the AC_{III} appears to be loose and porous. It is speculated that AC_{III} could have a better electrochemical performance as electrode materials. Furthermore, the TEM images of AC_{III} (Figure 1e,f) show that its amorphous structure has a large number of pores [21].

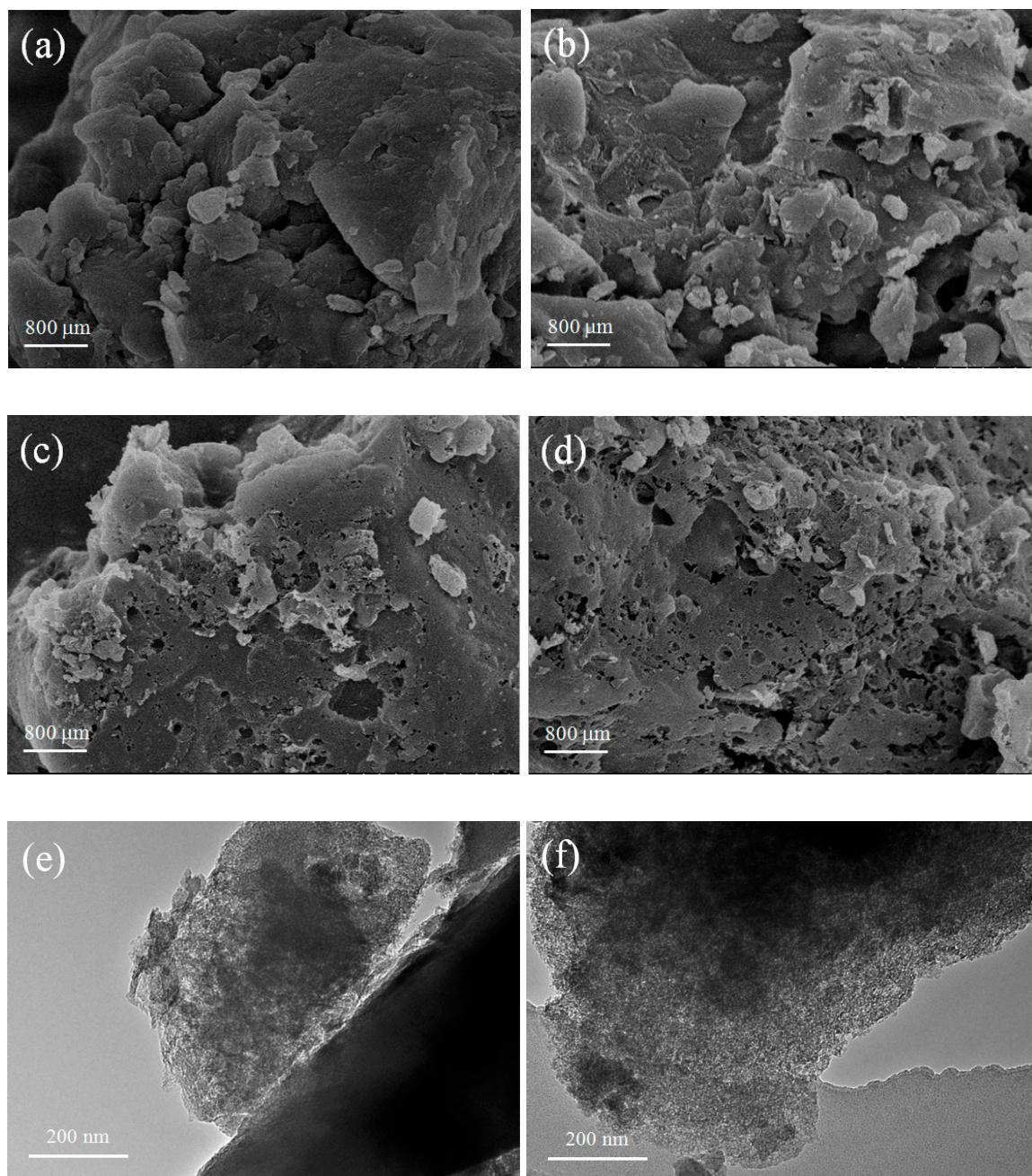


Figure 1. SEM images of Taixi anthracite (TXA) and activated carbons (ACs): (a) TXA; (b) AC_I; (c) AC_{II}; (d) AC_{III}; (e) and (f) TEM image of AC_{III}.

The XRD patterns of TXA, AC_I, AC_{II}, and AC_{III} are presented in Figure 2. Due to the high degree of coalification, the sharp peak of 26° and the weak peaks of 43° are shown in the XRD of TXA, corresponding to the reflection of the (002) plane and (100) plane of the aromatic layer, respectively, indicating the presence of a microcrystalline graphitized structure [20,27,28]. Compared with TXA, the peak of AC_I at $2\theta = 26^\circ$ becomes relatively gentle, indicating that the degree of graphitization of AC decreases after physical activation. In the XRD patterns of AC_{II} and AC_{III}, the (002) peak becomes weaker due to the internal erosion process of KOH activation [24,29], and the accumulation structure of the aromatic layer further changes to the amorphous structure, resulting in an increase in pores and facilitating the storage of charges. The small peak appeared at 44° of AC_{III} can be indexed to a superposition of the (101) reflections of the graphite structure [30]. This shows that AC_{III} after

three activations has a special structure between the disordered amorphous carbon phase and the graphitic phase.

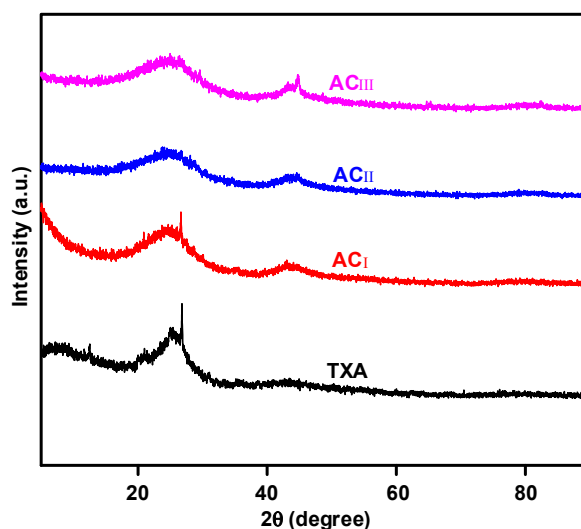


Figure 2. XRD patterns of TXA, AC_I, AC_{II} and AC_{III}.

The electrochemical properties of activated carbon are also affected by the functional groups on the surface. Therefore, FTIR tests were carried out on the samples. As shown in Figure 3, the absorption peaks at 2972 and 2920 cm^{-1} correspond to the stretching vibration of C-H [31], and the absorption peak at 1380 cm^{-1} corresponds to the in-plane bending vibration of C-H [32]. The absorption peaks at 845, 795, and 742 cm^{-1} conform to the out-of-plane bending vibration of C-H [33]. Moreover, the peak at about 1640 cm^{-1} is consistent with the stretching vibration of C=C, and the peak at 1610 cm^{-1} matches with the stretching vibration of the aromatic skeleton, indicating that there is a certain degree of graphitization structure in TXA, which is consistent with the analysis of XRD. It is found that after physical activation, the absorption peaks of ACFS at 1640 and 1610 cm^{-1} become weak, indicating that the activation process could reduce the graphitization degree of the sample, which is also confirmed in the XRD analysis. In addition, the absorbance for the aromatic skeleton stretching vibration in the FTIR spectrum is further weakening after chemical activation. All samples show a relatively wide band at 3430 cm^{-1} , corresponding to the stretching vibration of hydroxyl [32,34]. TXA has a distinct band at 1040 cm^{-1} , corresponding to the bending vibration of C-O [6], which gradually weakens in AC_I, AC_{II}, and AC_{III}, indicating partial cleavage of C-O bonds during activation.

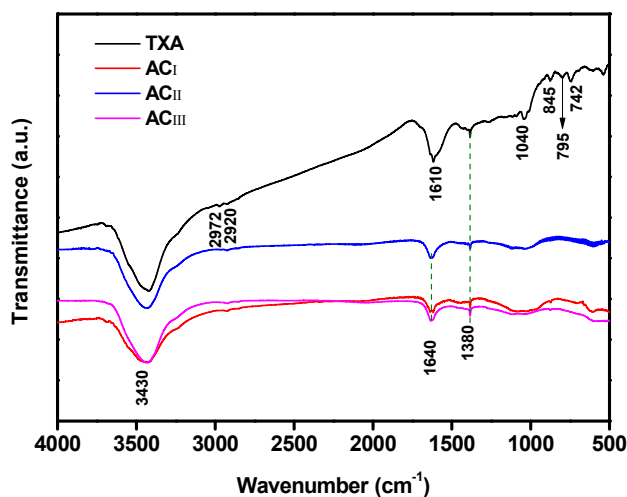


Figure 3. FTIR spectra of TXA, AC_I, AC_{II} and AC_{III}.

Two distinct peaks appear in the XPS spectra of TXA and the samples at approximately 285 and 532 eV, corresponding to C1s and O1s, as shown in Figure 4a. The C1s spectra of the samples are separated into four peaks by curve fitting, and are located at the binding energy of 284.8, 285.0, 286.4, and 288.9 eV, corresponding to C-C, C-O, C=O, and O-C=O functional groups [26,35]. This also proves the presence of oxygen-containing functional groups on the surface of the samples. It has been reported that the wettability of the material in aqueous solution is improved due to the presence of oxygen-containing functional groups [36,37], which also contributes to the improvement of the specific capacitance of the electrode.

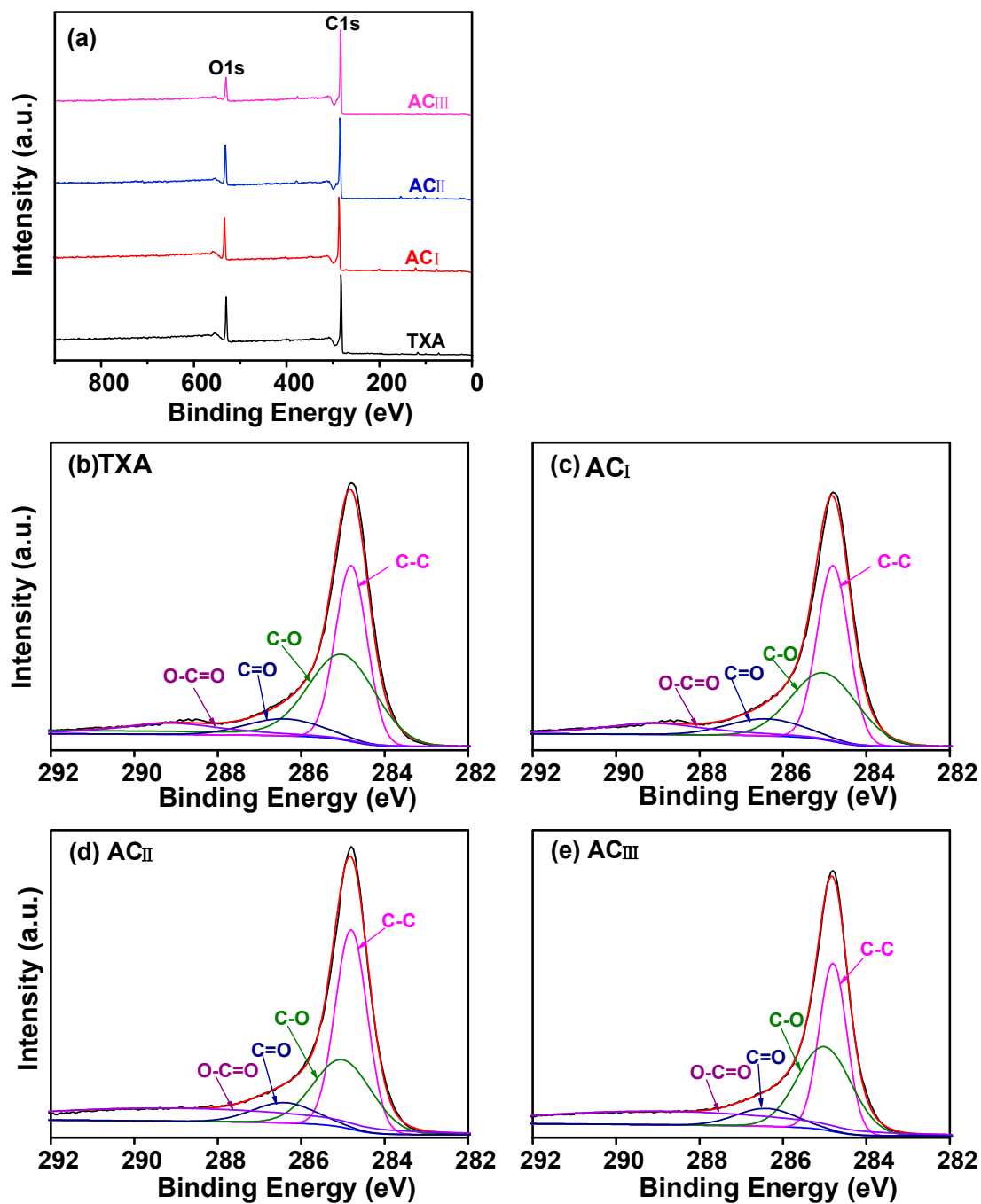


Figure 4. XPS survey spectra of ACs: (a) XPS wide scan spectra; (b–e) High resolution C1s spectra.

N_2 adsorption-desorption analysis of AC_I , AC_{II} and AC_{III} was performed, as shown in Figure 5a. According to the classification of International Union of Pure and Applied Chemistry (IUPAC), the N_2 adsorption-desorption isotherms of Acs belong to the combination of Type I isotherm and Type IV isotherm, indicating that there are a large number of micropores and a certain number of mesopore in the three samples [26]. The AC_{III} shows a large adsorption capacity in the range of low relative pressure and a very obvious H4 hysteresis loop in the range of 0.4 to 1 relative pressure, proving a large number of mesoporous pores in AC_{III} [24]. As illustrated in Figure 5b, most of the pore diameters of AC_I are below 1 nm and only a few pores diameters of AC_I range from 3 to 4 nm. The pore diameters of AC_{II} are bigger than AC_I in the range of 0.5–1 nm, revealing that the KOH exhibits a remarkable effect of hole-expanding during the first chemical activation. The pores of AC_{II} were further developed through the process of impregnation and chemical activation again to produce AC_{III} , not only the number of the pores with diameters of 0.5–2.5 nm increased, but also a large number of mesopores appeared at a diameter of 3–4 nm. Chmiola et al. found that the pores with diameters of 0.6–1 nm can effectively increase the specific capacitance [38]. Specific capacitance can be increased by increasing the number of micropores with suitable pore diameter. In addition, increasing the number of mesopores can effectively increase the ion diffusion channel, reduce the diffusion resistance and improve the utilization of micropores, thereby facilitating the electrochemical performance of the material [39].

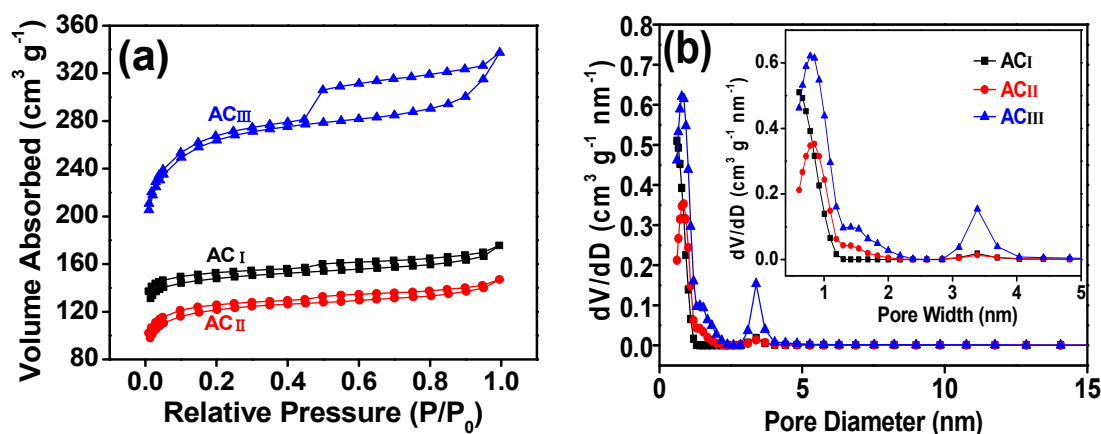


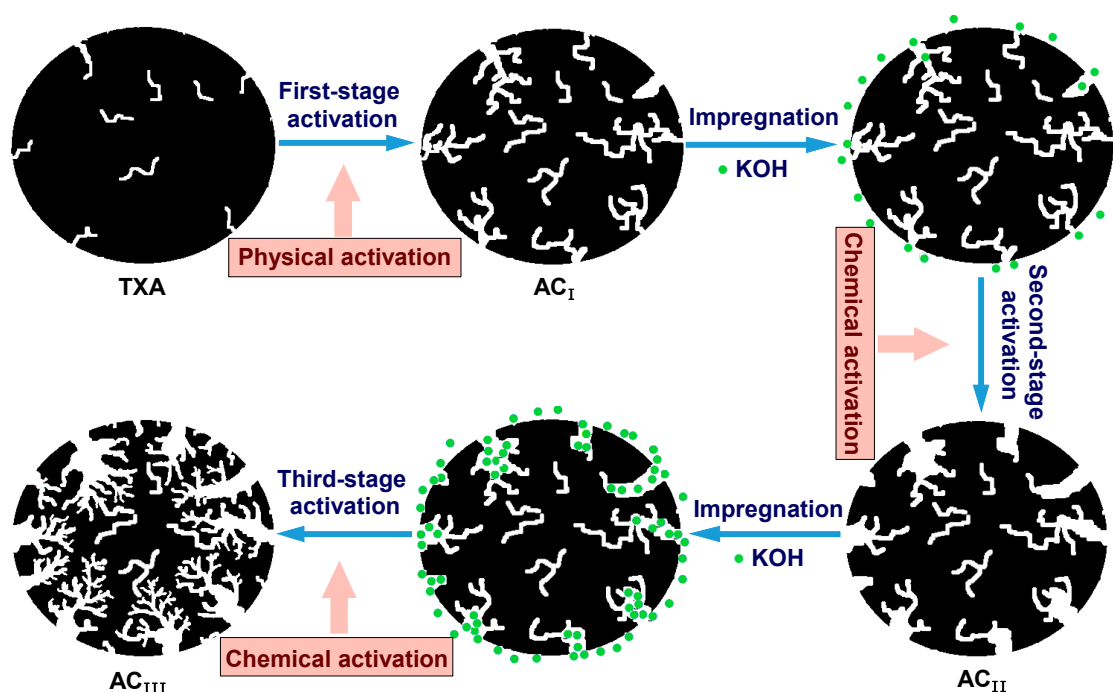
Figure 5. N_2 adsorption-desorption isotherms (a) and pore size distribution (b) of AC_I , AC_{II} and AC_{III} .

The pore structure parameters of the samples are listed in Table 1. Compared with AC_I , the specific surface area (S_{BET}) and micropore volume (V_{mic}) of AC_{II} are reduced, but the mesopore volume (V_{mes}) and average pore diameter (D_{ap}) are increased, indicating that the carbon in the inner wall of the micropores reacts with KOH to enlarge the pore diameter through one-stage activation. The largest contribution to surface area is micropores. In other words, the more micropores of the same quality sample are available, the larger the specific surface area it has. So AC_{II} has more mesopores and macropores than AC_I , and a larger average pore diameter than AC_I , but the specific surface area of AC_{II} is smaller than AC_I , because AC_I has more micropores than AC_{II} . The S_{BET} , total pore volume (V_t), V_{mic} and V_{mes} of AC_{III} are obviously increased, proving that the AC which has undergone impregnation and chemical activation again exhibits more abundant pores, including the enlargement of small pores and generation of new pores. This is consistent with previous SEM analysis.

Table 1. The pore structure parameters of TXA and ACs.

Samples	S_{BET} ($m^2 g^{-1}$)	V_t ($cm^3 g^{-1}$)	V_{mic} ($cm^3 g^{-1}$)	V_{mes} ($cm^3 g^{-1}$)	V_{mes}/V_t (%)	D_{ap} (nm)
AC_I	591.3	0.2715	0.2263	0.0156	16.7	1.84
AC_{II}	466.1	0.2274	0.2058	0.0216	18.7	1.95
AC_{III}	984.6	0.5219	0.3993	0.1226	23.5	2.12

The pore structure of electrode materials has a great influence on electrochemical characteristics. The macropore, like a reservoir, is the place where ions are stored, and the mesopore is the channel for ions to be transported rapidly, moreover, the micropore provides the place for effective charge accumulation. The macropore, mesopore, and micropore are responsible for each other. Therefore, appropriate pore size distribution is conducive to improving the capacitance. As shown in Scheme 1, the raw coal itself has fewer pores. A large number of pores are formed in AC_I by one-stage activation, which is mainly microporous, but the few mesopores and macropores that appear in ions cannot move rapidly enough. In the second stage, KOH is impregnated into the pores of the AC_I, while more pores with larger pore sizes were generated through the reaction of KOH with the carbon on the pore walls after second-stage activation. Therefore, the mesoporosity of AC_{II} increases. In the third stage, more KOH enter into the pores of AC_{II} through impregnation and react with the carbon on the pore walls of AC_{II}. After that, part of the micropores of AC_{II} are reamed to form mesopores, and a large number of new, deeper and more developed micropores are generated around the mesopores. The specific surface area of the activated carbon increased from 591.3 m² g⁻¹ to 984.6 m² g⁻¹ after being activated twice.



Scheme 1. Schematic of the synthesis strategy of ACs.

The possible pathways for preparation strategy of AC and pore formation were proposed based on the above characterizations, as displayed in Scheme 1. Firstly, TXA was physically activated with CO₂ to obtain AC_I, which has a certain amount of micropores and a small amount of mesopores. Secondly, AC_I was impregnated in KOH solution, while K⁺ was attaching to the surface of AC_I and partly entering into the larger diameter pores. Then AC_I was chemically activated to produce AC_{II}, and the pore size of AC_{II} increased obviously due to K⁺ etching. After the impregnation treatment for AC_{II}, the pore structure was further developed in the subsequent chemical activation process because of the larger pore, leading to transferring more K⁺ into its interior structures. In addition, the use of the impregnation method can make the K⁺ relatively uniform into the pores of the ACs, which may reduce the local excessive etching and the pore collapse due to the uneven distribution of K⁺. The AC_{III} with more mesopores and high specific surface area was prepared through three-step activation.

2.2. Electrochemical Performance

The electrochemical properties of AC_I, AC_{II}, and AC_{III} were evaluated by galvanostatic charge-discharge (GCD), cyclic voltammetry (CV), and electrochemical impedance spectroscopy (EIS) tests with a 6 mol L⁻¹ KOH aqueous solution as electrolyte solution in the three-electrode system. The GCD curves of the three samples at 1 A g⁻¹ current density, as taken in Figure 6a, show that all curves are highly symmetric triangles, indicating that the electrode materials have typical double layer capacitor characteristics and good electrochemical reversibility [40,41]. Clearly, AC_{III} shows the longest discharge time, indicating that it has the largest specific capacitance among the three samples under the same test conditions [42,43]. Besides, according to the Equation (1), the specific capacitances of AC_I, AC_{II}, and AC_{III} at 1 A g⁻¹ are 81, 106, and 199 F g⁻¹, respectively. Compared with AC_I and AC_{II}, AC_{III} has a significant increase in specific capacitance, which is 2.45 times that of ACSF and 1.88 times that of AC_{II}, proving the importance of re-impregnation and activation of activated carbon. In addition, the voltage drop of the three activated carbon samples at a current density of 1 A g⁻¹ are shown in Figure 6b. The voltage drops of AC_I, AC_{II}, and AC_{III} are 0.0312, 0.0275, and 0.0148 V, respectively, and the values decrease in turn, indicating that the internal resistance of the electrode is reduced [21]. This may be related to the fact that multiple activation increases the pore size and reduces the diffusion resistance. Magnification performance is one of the key factors affecting the practical application of electrode materials. The specific capacitances of AC_I, AC_{II}, and AC_{III} at different current densities are shown in Figure 6c. It is clear that at the same current density, the specific capacitance of AC_{III} is much higher than AC_I and AC_{II}, reaching 206 F g⁻¹ at 0.5 A g⁻¹. Even if the current density reaches 5 A g⁻¹, the specific capacitance of AC_{III} is still 190 F g⁻¹, showing excellent rate performance. This is due to the more reasonable pore size distribution of AC_{III}, especially the increase of mesopores, which is conducive to the rapid transmission of electrolyte ions.

Figure 6d shows the CV curves for all samples at a scan rate of 10 mV s⁻¹. All curves exhibit an approximately rectangular character, exhibiting excellent capacitive behavior, which illustrates that the capacitance of all samples is primarily derived from the electrical double-layer capacitance behavior [44–46]. Moreover, it is observed that the CV curve has a certain degree of distortion, which is due to the pseudo capacitance effect provided by the fast redox reaction of oxygen-containing functional groups [47]. It is well known that the integral area of the CV curve corresponds to the capacitance of the supercapacitor. Therefore, AC_{III} has the largest specific capacitance at the same scanning rate. Besides, the CV curve of AC_{III} at a scan rate of 5 to 100 mV s⁻¹ is exhibited in Figure 6e. Even at relatively high scan rates, the CV curve of AC_{III} remains approximately rectangular, exhibiting good electrochemical behavior, due to the presence of a large number of mesopores facilitating the rapid transmission of electrolyte ions within the pores, which is in accordance with the analysis of GCD.

In order to make further evaluation of the ACs performance as electrode materials of supercapacitors, EIS analysis are performed. Figure 6f is the Nyquist plots of the samples, in which the illustration is an enlarged view of the high frequency region. Clearly, all curves show a diagonal line in the low frequency region and a semicircle in the high frequency region. In general, the slope of the linear portion of the Nyquist diagram in the low frequency region is related to the diffusion resistance caused by the diffusion/transmission of the electrolyte ions in the electrolyte and the electrode material, and the larger the slope, the closer the supercapacitor is to the ideal capacitor behavior [48–50]. Then the slope of AC_{III} is obviously greater than that of AC_I and AC_{II}, indicating that AC_{III} has smaller diffusion resistance, which is consistent with the analysis of N₂ adsorption and desorption test. The diameter of the semicircle in the high frequency region corresponds to the charge transfer resistance (R_{ct}) [51,52]. It is clear that the R_{ct} of AC_I, AC_{II}, and AC_{III} in the illustration in Figure 6f increases sequentially, due to the decrease in the degree of graphitization of AC during the activation process, which is in accord with the XRD analysis. In addition, the solution resistance (R_s) can be obtained from the Z' axis intercept of the Nyquist plot [4], and the R_s values of all samples are very small, which also reflects the excellent electrochemical performance of the prepared materials. The cyclic stability is also an important index for evaluating the performance of supercapacitors. Therefore, the 5000 GCD cycle tests were executed

for AC_{III} at 1 A g⁻¹, as shown in Figure 7. It is worth noting that in the first 200 cycles, the specific capacitance of AC_{III} increases significantly, indicating that the AC electrodes undergo electrochemical activation in the incipient charge and discharge processes. And during electrochemical activation, the suitable charge-discharge cycles can promote the electrolyte ions to be completely inserted into the pores of AC, thus improving the availability of the surface area of the charge storage [53]. More impressively, the specific capacitance of the AC_{III} remained at 98.1% of the initial value after 5000 cycles, showing excellent cycle performance. Based on the above analysis, AC_{III} exhibits relatively high specific capacitance, excellent rate performance, and reliable cycle stability, which is more in line with practical application requirements.

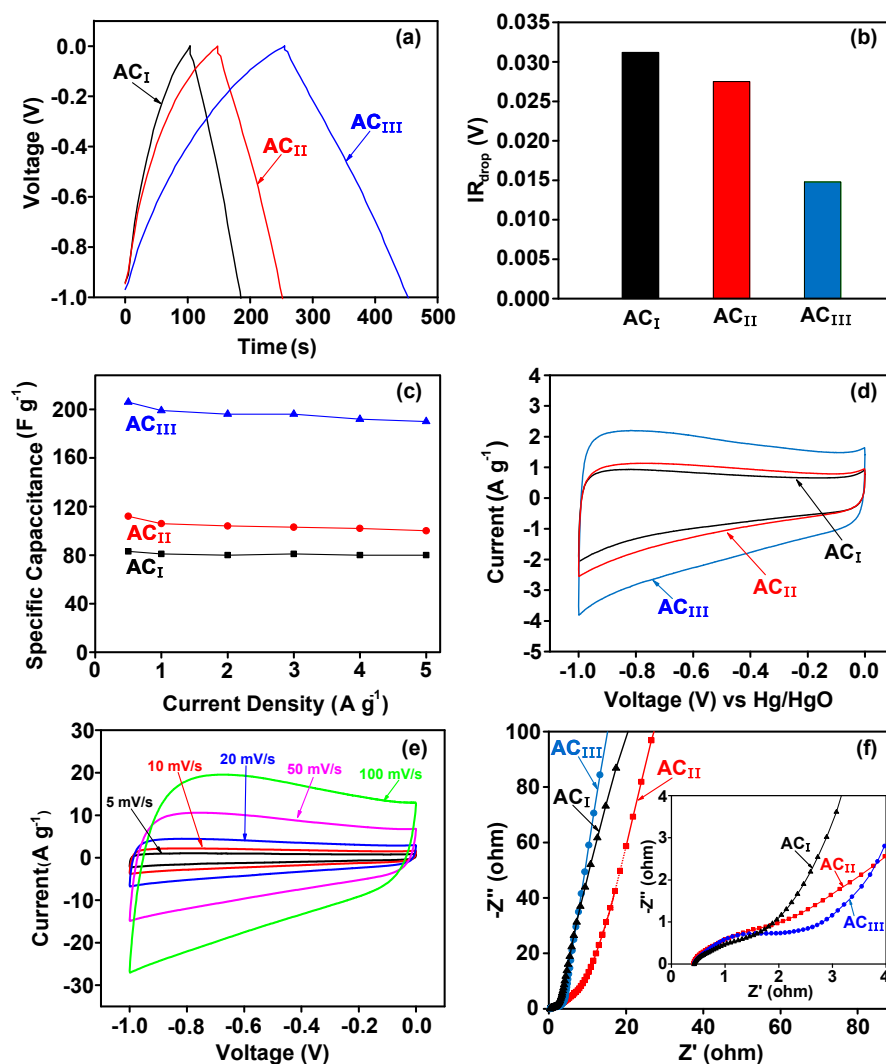


Figure 6. (a) Galvanostatic charge-discharge (GCD) curves of AC electrodes in 6 M KOH electrolyte at 1 A g⁻¹; (b) The voltage drops of AC electrodes at 1 A g⁻¹; (c) Specific capacitance of AC electrodes at different current densities; (d) CV curves of AC electrodes at 10 mV s⁻¹; (e) CV curves of AC_{III} electrodes at different scan rates; (f) Nyquist plots of AC electrodes.

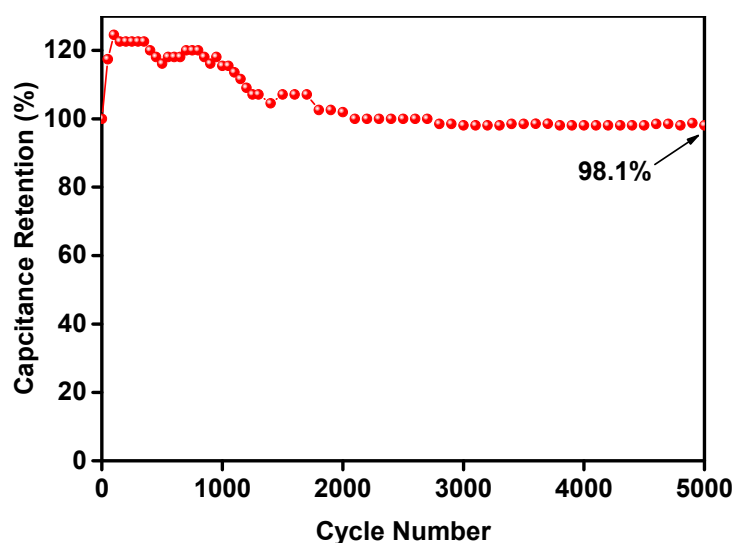


Figure 7. Cycle stability of AC_{III} electrodes measured at 1 A g⁻¹.

3. Materials and Methods

3.1. Materials

Anthracite collected from Taixi, Ningxia province was taken as the precursor of ACs. Its proximate and ultimate analyses are shown in Table 2. Coal tar as the binder of columnar ACs was purchased from Jiangsu Weitian Chemical Group Company. KOH and hydrochloric acid used in the experiment were purchased from Sinopharm Chemical Reagent Co., Ltd. Acetylene black, anhydrous ethanol and potassium nitrate were purchased from Xiqiao Chemical Co., Ltd. All chemical reagents were of analytical grade and used directly without further purification.

Table 2. Proximate and ultimate analyses of Taixi anthracite.

Proximate Analysis (wt.%)				Ultimate Analyses (wt.%, daf)				
M_{ad}	A_d	VM_{daf}	FC_{daf}^a	C	H	O ^a	N	S
1.45	3.88	7.67	92.33	94.67	2.49	1.90	0.75	0.19

ad: air dry basis; d: dry basis; daf: dry and ash-free basis.^a By difference.

3.2. Preparation of AC

3.2.1. Pretreatment of TXA

TXA was crushed and ground to below 200 mesh. Then 100 g TXA thoroughly stirred by adding 2 g KNO₃, 32.5 g coal tar and 5 ml deionized water. After that, it was pressed into cylindrical strips having a diameter of 2.8 mm by a plodder. Finally, the strips were naturally dried and broken until they were 1–2 cm long.

3.2.2. The First-Stage Activation by Physical Activation

The treated strip was put into muffle furnace at room temperature and heated at 12 °C min⁻¹ to 600 °C under nitrogen flow for carbonization. After carbonization, the sample was activated with CO₂ as activator in a horizontal tube furnace with a heating rate of 12 °C min⁻¹ from room temperature to 900 °C, and kept at 900 °C for 2 h. The sample was cooled to room temperature and then washed several times with 1 mol L⁻¹ HCl solution, followed by washing with deionized water until the solution was neutral. Afterwards, the sample was dried at 80 °C for 24 h and denoted as the first-stage activated carbon (AC_I).

3.2.3. The Second-Stage Activation by Chemical Activation

AC_I was impregnated in 12 mol L⁻¹ KOH solution and magnetically stirred for 24 h at room temperature. The sample was then filtered and dried at 80 °C for 24 h. In addition, the sample was weighed before and after immersion, and the corresponding mass ratio of alkali to carbon was about 1:3 by difference method. After that, the sample was placed in a tube furnace with N₂ as a shielding gas and heated from room temperature to 800 °C at 12 °C min⁻¹ for 1 h. Then the activated sample was cooled to room temperature and washed several times with 1 mol L⁻¹ HCl solution, followed by washing with deionized water until the solution was neutral. The resulting columnar AC was then dried at 80 °C for 24 h and denoted as activated carbon from the second-stage activation (AC_{II}).

3.2.4. The Third-Stage Activation by Chemical Activation

The procedure described in 2.2.3 for AC_{II} was repeated and the resulting AC was recorded as activated carbon for the third stage (AC_{III}).

3.3. Characterizations

The microstructure of ACs was analyzed by scanning electron microscopy (SEM, Hitachi, Su8020) with a field emission scanning electron microanalyzer at 5 kV. Transmission electron microscope measurements were carried out on a microscope (TEM, FEI, Tecnai G2 F20) at 200 kV. X-ray diffraction (XRD) analysis was performed at 40 kV and 30 mA using a Bruker D8 Advance diffractometer with a Cu K α X-ray source, the scan range was between 5 and 90°. Fourier transform infrared (FTIR) spectra of the samples were obtained by a Nicolet is 5 infrared spectrometer by using pressed KBr pellets. X-ray photoelectron spectroscopy (XPS) was implemented on an ESCALAB 250Xi (Thermo Fisher) instrument with monochromatized Al K α probe beam. The energy scale was corrected with C1s peak at 284.8 eV as internal standard. The transmit power is 250 W and it was used for wide-range scanners and narrow scans over the ranges of 0–900 eV and 282–292 eV respectively, at a pass energy of 100 eV and 20 eV, respectively. The background was subtracted use a function of Shirley. The N₂ adsorption-desorption isotherm was measured at 77 K using an Autosorb-1 type adsorbent manufactured by Quantachrome, and the specific surface areas (S_{BET}) were calculated by the Brunauer-Emmett-Teller (BET) equation. The total pore volume (V_t) of the sample was calculated from the relative pressure (P/P_0) of 0.99. The pore size distribution was calculated by density functional theory (DFT). The average pore diameter (D_{ap}) of the sample was calculated from Equation (1).

$$D_{ap} = \frac{4V_t}{S_{BET}} \quad (1)$$

3.4. Electrochemical Measurement

Briefly, the AC we prepared was pulverized to pass through a 200-mesh sieve. 20 mg AC powder, 2.5 mg acetylene black, and 2.5 mg polytetrafluoroethylene were mixed into ethanol, followed by ultrasonic treatment for 5 min. Then the mixture was uniformly applied to long strips of foamed nickel, and dried in vacuum at 80 °C for 24 h. The active mass of the electrode was ca. 2 mg cm⁻². All samples were electrochemically tested in a 6 mol/L KOH solution with nickel foam coated with ACs as working electrode, platinum sheet as the counter electrode, and Hg/HgO electrode as the reference electrode.

The GCD tests were performed at room temperature using a NEWARE BTS high precision battery detection system at a current density of 0.5–5 A g⁻¹. Cyclic voltammetry (CV) tests were measured using a CHI66D electrochemical workstation (CH Instrument, Shanghai, China) at a voltage range of –1 to 0 V. Electrochemical impedance spectroscopy (EIS) measurements were conducted at an open circuit potential with an AC amplitude of 10 mV over a frequency range of 1 mHz to 100 kHz. The specific capacitance under three-electrode system was calculated according to Equation (2):

$$C = \frac{I\Delta t}{m\Delta V} \quad (2)$$

where I (A) is the discharge current; m (g) is the mass of the AC; Δt (s) is the discharge time interval; ΔV (V) is the voltage difference during the corresponding discharge time.

4. Conclusions

In conclusion, a lot of micropores in AC_I were generated through carbonization and physical activation with CO₂ as an activator. The volumes of micropores and mesopores in AC_{III} were increased significantly more than that in AC_I after two impregnations of KOH solution and two activations at 800 °C for 1 h. When using the ACs as active substances in the three-electrode system, the specific capacitance of AC_{III} was 206 F g⁻¹ at 0.5 A g⁻¹, much higher than AC_I and AC_{II}. It shows higher specific capacitance, excellent rate performance, and good cycling stability of AC_{III}. In addition, the impregnation method can reduce the dosage of KOH and reduce the corrosion of equipment during the activation process. The method adopted in this paper may pave the way for industrial production of carbon-based electrode materials for high high-performance supercapacitors.

Author Contributions: X.-M.Y. and S.-Q.Z. designed the experiment, supervised the work and revised the manuscript; Z.-Y.A. and Y.-J.H. performed the experiments; Z.-Y.A. wrote the paper; M.Y., C.-C.X. and Z.-J.L. carried out for characterization; Y.H. and J.-S.Z. contributed to commented the manuscript. All authors have read and approved the manuscript.

Funding: This work was supported by the National Key Research and Development Program of China (2018YFC0604705), Fundamental Research Fund for the Central Universities (China University of Mining & Technology, Grant 2013QNA16), National Natural Science Foundation of China (Grant 51974302).

Conflicts of Interest: The authors declare no competing financial interest.

References

1. Long, C.; Xiao, Y.; Zheng, M.T.; Hu, H.; Dong, H.W.; Lei, B.F.; Zhang, H.R.; Zhuang, J.L.; Liu, Y.L. Synthesis of hybrid Ni-Co oxide @ 3D carbon skeleton derived from pollen grains for advanced supercapacitors. *Electrochim. Acta* **2016**, *210*, 695–703. [[CrossRef](#)]
2. Geuli, O.; Hao, Q.L.; Mandler, D. One-step fabrication of NiOx-decorated carbon nanotubes-NiCo₂O₄ as an advanced electroactive composite for supercapacitors. *Electrochim. Acta* **2019**, *318*, 51–60. [[CrossRef](#)]
3. Hao, L.; Li, X.L.; Zhi, L.J. Carbonaceous electrode materials for supercapacitors. *Adv. Mater.* **2013**, *25*, 3899–3904. [[CrossRef](#)] [[PubMed](#)]
4. Zhang, L.; Li, T.H.; Ji, X.G.; Zhang, Z.Y.; Yang, W.B.; Gao, J.J.; Li, H.; Xiong, C.Y.; Dang, A. Freestanding three-dimensional reduced graphene oxide/MnO₂ on porous carbon/nickel foam as a designed hierarchical multihole supercapacitor electrode. *Electrochim. Acta* **2017**, *252*, 306–314. [[CrossRef](#)]
5. Zhang, L.L.; Zhao, X.S. Carbon-based materials as supercapacitor electrodes. *Chem. Soc. Rev.* **2009**, *38*, 2520–2531. [[CrossRef](#)] [[PubMed](#)]
6. Liu, R.H.; Liu, E.H.; Ding, R.; Liu, K.; Teng, Y.; Luo, Z.Y.; Li, Z.P.; Hu, T.T.; Liu, T.T. Facile in-situ redox synthesis of hierarchical porous activated carbon@MnO₂ core/shell nanocomposite for supercapacitors. *Ceram. Int.* **2015**, *41*, 12734–12741. [[CrossRef](#)]
7. Wang, J.W.; Chen, Y.; Chen, B.Z. A Synthesis Method of MnO₂/Activated Carbon Composite for Electrochemical Supercapacitors. *J. Electrochem. Soc.* **2015**, *162*, A1654–A1661. [[CrossRef](#)]
8. Yin, L.H.; Chen, Y.; Li, D.; Zhao, X.Q.; Hou, B.; Cao, B.K. 3-Dimensional hierarchical porous activated carbon derived from coconut fibers with high-rate performance for symmetric supercapacitors. *Mater. Design* **2016**, *111*, 44–50. [[CrossRef](#)]
9. Geng, X.; Li, L.X.; Li, F. Carbon nanotubes/activated carbon hybrid with ultrahigh surface area for electrochemical capacitors. *Electrochim. Acta* **2015**, *168*, 25–31. [[CrossRef](#)]
10. Jin, Z.; Yan, X.D.; Yu, Y.H.; Zhao, G.J. Sustainable activated carbon fibers from liquefied wood with controllable porosity for high-performance supercapacitors. *J. Mater. Chem. A* **2014**, *2*, 11706–11715. [[CrossRef](#)]
11. Qin, K.; Kang, J.; Li, J.; Shi, C.; Li, Y.; Qiao, Z.; Zhao, N. Free-standing porous carbon nanofiber/ultrathin graphite hybrid for flexible solid-state supercapacitors. *ACS Nano* **2015**, *9*, 481–487. [[CrossRef](#)] [[PubMed](#)]

12. Bai, C.H.; Sun, S.G.; Xu, Y.Q.; Yu, R.J.; Li, H.J. Facile one-step synthesis of nanocomposite based on carbon nanotubes and Nickel-Aluminum layered double hydroxides with high cycling stability for supercapacitors. *J. Colloid Interf. Sci.* **2016**, *480*, 57–62. [[CrossRef](#)] [[PubMed](#)]
13. Liu, W.; Tang, Y.K.; Sun, Z.P.; Gao, S.S.; Ma, J.H.; Liu, L. A simple approach of constructing sulfur-containing porous carbon nanotubes for high-performance supercapacitors. *Carbon.* **2017**, *115*, 754–762. [[CrossRef](#)]
14. Ling, Z.; Wang, Z.Y.; Zhang, M.D.; Yu, C.; Wang, G.; Dong, Y.F.; Liu, S.H.; Wang, Y.W.; Qiu, J.S. Sustainable Synthesis and Assembly of Biomass-Derived B/N Co-Doped Carbon Nanosheets with Ultrahigh Aspect Ratio for High-Performance Supercapacitors. *Adv. Funct. Mater.* **2016**, *26*, 111–119. [[CrossRef](#)]
15. Chen, C.; Yu, D.F.; Zhao, G.Y.; Du, B.S.; Tang, W.; Sun, L.; Sun, Y.; Besenbacher, F.; Yu, M. Three-dimensional scaffolding framework of porous carbon nanosheets derived from plant wastes for high-performance supercapacitors. *Nano Energy* **2016**, *27*, 377–389. [[CrossRef](#)]
16. Pan, Z.H.; Zhi, H.Z.; Qiu, Y.C.; Yang, J.; Xing, L.D.; Zhang, Q.C.; Ding, X.Y.; Wang, X.S.; Xu, G.G.; Yuan, H. Achieving commercial-level mass loading in ternary-doped holey graphene hydrogel electrodes for ultrahigh energy density supercapacitors. *Nano Energy* **2018**, *46*, 266–276. [[CrossRef](#)]
17. Shao, Y.; Elkady, M.F.; Wang, L.J.; Zhang, Q.; Li, Y.; Wang, H.; Mousavi, M.F.; Kaner, R.B. Graphene-based materials for flexible supercapacitors. *Chem. Soc. Rev.* **2015**, *44*, 3639–3665. [[CrossRef](#)]
18. Abdelhamid, A.A.; Yang, X.; Yang, J.; Chen, X.; Ying, J.Y. Graphene-wrapped nickel sulfide nanoprisms with improved performance for Li-ion battery anodes and supercapacitors. *Nano Energy* **2016**, *26*, 425–437. [[CrossRef](#)]
19. Xing, B.L.; Guo, H.; Chen, L.J.; Chen, Z.F.; Zhang, C.X.; Huang, G.X.; Xie, W.; Yu, J.L. Lignite-derived high surface area mesoporous activated carbons for electrochemical capacitors. *Fuel Process. Technol.* **2015**, *138*, 734–742. [[CrossRef](#)]
20. Dong, S.A.; Ji, X.Y.; Yu, M.X.; Xie, Y.Y.; Zhang, D.W.; He, X.J. Direct synthesis of interconnected porous carbon nanosheet/nickel foam composite for high-performance supercapacitors by microwave-assisted heating. *J. Porous Mater.* **2018**, *25*, 923–933. [[CrossRef](#)]
21. Qin, B.; Wang, Q.; Zhang, X.H.; Xie, X.L.; Jin, L.; Cao, Q. One-pot synthesis of interconnected porous carbon derived from coal tar pitch and cellulose for high-performance supercapacitors. *Electrochim. Acta* **2018**, *283*, 655–663. [[CrossRef](#)]
22. Wang, L.X.; Wang, R.R.; Zhao, H.Y.; Liu, L.; Jia, D.Z. High rate performance porous carbon prepared from coal for supercapacitors. *Mater. Lett.* **2015**, *149*, 85–88. [[CrossRef](#)]
23. Abudu, P.; Wang, L.X.; Xu, M.J.; Jia, D.Z.; Wang, X.C.; Jia, L.X. Hierarchical porous carbon materials derived from petroleum pitch for high-performance supercapacitors. *Chem. Phys. Lett.* **2018**, *702*, 1–7. [[CrossRef](#)]
24. Xie, X.Y.; Dong, S.A.; Xiao, N.; Qiu, J.S.; He, X.J.; Shao, X.L. Synthesis of layered microporous carbons from coal tar by directing, space-confinement and self-sacrificed template strategy for supercapacitors. *Electrochim. Acta* **2017**, *246*, 634–642. [[CrossRef](#)]
25. Zhang, W.L.; Zhao, M.Z.; Liu, R.Y.; Wang, X.F.; Lin, H.B. Hierarchical porous carbon derived from lignin for high performance supercapacitor. *Colloid. Surface A* **2015**, *484*, 518–527. [[CrossRef](#)]
26. Xing, B.L.; Huang, G.X.; Chen, Z.F.; Chen, L.J.; Yi, G.Y.; Zhang, C.X. Facile preparation of hierarchical porous carbons for supercapacitors by direct carbonization of potassium humate. *J. Solid State Electro.* **2017**, *21*, 263–271. [[CrossRef](#)]
27. Xu, L.S.; Jia, M.Y.; Li, Y.; Jin, X.J.; Zhang, F. High-performance MnO₂-deposited graphene/activated carbon film electrodes for flexible solid-state supercapacitor. *Sci. Rep.-UK* **2017**, *7*, 12857. [[CrossRef](#)]
28. Choi, P.R.; Kim, S.G.; Jung, J.C.; Kim, M.S. High-energy-density activated carbon electrode for organic electric-double-layer-capacitor using carbonized petroleum pitch. *Carbon Lett.* **2017**, *22*, 70–80.
29. Yin, J.; Zhang, D.Y.; Zhao, J.Q.; Wang, X.L.; Zhu, H.; Wang, C.Y. Meso- and micro-porous composite carbons derived from humic acid for supercapacitors. *Electrochim. Acta* **2014**, *136*, 504–512. [[CrossRef](#)]
30. Shang, S.M.; Yang, X.M.; Tao, X.M. Easy synthesis of carbon nanotubes with polypyrrole nanotubes as the carbon precursor. *Polymer* **2009**, *50*, 2815–2818. [[CrossRef](#)]
31. Chen, Y.Y.; Dhaiveegan, P.; Michalska, M.; Lin, J.Y. Morphology-controlled synthesis of nanosphere-like NiCo₂S₄ as cathode materials for high-rate asymmetric supercapacitors. *Electrochim. Acta* **2018**, *274*, 208–216. [[CrossRef](#)]

32. Chen, H.Y.; Ai, Y.N.; Liu, F.; Chang, X.; Xue, Y.; Huang, Q.; Wang, C.; Lin, H.L.; Han, S. Carbon-coated Hierarchical Ni-Mn Layered Double Hydroxide Nanoarrays on Ni Foam for Flexible High-capacitance Supercapacitors. *Electrochim. Acta* **2016**, *213*, 55–65. [[CrossRef](#)]
33. Zhang, X.M.; Ma, J.; Yang, W.L.; Gao, Z.; Wang, J.; Liu, Q.; Liu, J.Y.; Jing, X.Y. Manganese dioxide core-shell nanowires in situ grown on carbon spheres for supercapacitor application. *CrystEngComm* **2014**, *16*, 4016–4022. [[CrossRef](#)]
34. Hao, X.Q.; Jiang, Z.Q.; Tian, X.N.; Hao, X.G.; Jiang, Z.J.; Hao, X.Q.; Jiang, Z.Q.; Tian, X.N.; Hao, X.G.; Jiang, Z.J. Facile Assembly of Co-Ni Layered Double Hydroxide Nanoflakes on Carbon Nitride Coated N-doped Graphene Hollow Spheres with High Electrochemical Capacitive Performance. *Electrochim. Acta* **2017**, *253*, 21–30. [[CrossRef](#)]
35. Pham, V.H.; Dickerson, J.H. Reduced Graphene Oxide Hydrogels Deposited in Nickel Foam for Supercapacitor Applications: Toward High Volumetric Capacitance. *J. Phy. Chem. C* **2016**, *120*, 5353–5360. [[CrossRef](#)]
36. He, X.J.; Zhang, N.; Shao, X.L.; Wu, M.B.; Yu, M.X.; Qiu, J.H. A layered- template-nanospace-confinement strategy for production of corrugated graphene nanosheets from petroleum pitch for supercapacitors. *Chem. Eng. J.* **2016**, *297*, 121–127. [[CrossRef](#)]
37. Li, J.; Liu, K.; Gao, X.; Yao, B.; Huo, K.; Cheng, Y.; Cheng, X.; Chen, D.; Wang, B.; Ding, D. Oxygen and nitrogen enriched 3D porous carbon for supercapacitors of high volumetric capacity. *ACS Appl. Mater. Inter.* **2015**, *7*, 24622–24628. [[CrossRef](#)]
38. Chmiola, J.; Yushin, G.; Gogotsi, Y.; Portet, C.; Simon, P.; Taberna, P.L. Anomalous increase in carbon capacitance at pore sizes less than 1 nanometer. *Science* **2006**, *313*, 1760–1763. [[CrossRef](#)]
39. He, X.J.; Li, X.J.; Ma, H.; Han, J.F.; Zhang, H.; Yu, C.; Xiao, N.; Qiu, J.S. ZnO template strategy for the synthesis of 3D interconnected graphene nanocapsules from coal tar pitch as supercapacitor electrode materials. *J. Power Sources* **2017**, *340*, 183–191. [[CrossRef](#)]
40. Han, S.S.; Hou, F.; Yuan, X.B.; Liu, J.C.; Yan, X.; Chen, S.Q. Continuous hierarchical carbon nanotube/reduced graphene oxide hybrid films for supercapacitors. *Electrochim. Acta* **2017**, *225*, 566–573. [[CrossRef](#)]
41. Li, Z.; Xu, Z.W.; Wang, H.L.; Ding, J.; Zahiri, B.; Holt, C.M.B.; Tan, X.H.; Mitlin, D. Colossal pseudocapitance in a high functionality-high surface area carbon anode doubles the energy of an asymmetric supercapacitor. *Energ. Environ. Sci.* **2014**, *7*, 1708–1718. [[CrossRef](#)]
42. Zhang, Z.Q.; Zhang, H.D.; Zhang, X.Y.; Yu, D.Y.; Ji, Y.; Sun, Q.S.; Wang, Y.; Liu, X.Y. Facile synthesis of hierarchical CoMoO₄@NiMoO₄ core-shell nanosheet arrays on nickel foam as an advanced electrode for asymmetric supercapacitors. *J. Mater. Chem. A* **2016**, *4*, 18578–18584. [[CrossRef](#)]
43. Li, Y.; Xu, Z.Y.; Wang, D.W.; Zhao, J.; Zhang, H.H. Snowflake-like core-shell α -MnO₂@ δ -MnO₂ for high performance asymmetric supercapacitor. *Electrochim. Acta* **2017**, *251*, 344–354. [[CrossRef](#)]
44. Yan, J.; Wang, Q.; Wei, T.; Fan, Z.J. Recent Advances in Design and Fabrication of Electrochemical Supercapacitors with High Energy Densities. *Adv. Energy Mater.* **2014**, *4*, 157–164. [[CrossRef](#)]
45. Shao, J.Q.; Ma, F.W.; Wu, G.; Dai, C.C.; Geng, W.D.; Song, S.J.; Wan, J.F. In-situ MgO (CaCO₃) templating coupled with KOH activation strategy for high yield preparation of various porous carbons as supercapacitor electrode materials. *Chem. Eng. J.* **2017**, *321*, 301–313. [[CrossRef](#)]
46. Das, T.; Chauhan, H.; Deka, S.; Chaudhary, S.; Boruah, R.; Saikia, B.K. Promising carbon nanosheet-based supercapacitor electrode materials from low-grade coals. *Micropor. Mesopor. Mater.* **2017**, *253*, 80–90. [[CrossRef](#)]
47. Shao, J.; Zhou, X.; Liu, Q.; Zou, R.; Li, W.; Yang, J.; Hu, J. Mechanism analysis of the capacitance contributions and ultralong cycling-stability of the isomorphous MnO₂@MnO₂ core/shell nanostructures for supercapacitors. *J. Mater. Chem. A* **2015**, *3*, 6168–6176. [[CrossRef](#)]
48. Li, S.F.; Yu, C.; Yang, J.; Zhao, C.T.; Fan, X.M.; Huang, H.W.; Han, X.T.; Wang, J.X.; He, X.J.; Qiu, J.H. Ultrathin Nitrogen-Enriched Hybrid Carbon Nanosheets for Supercapacitors with Ultrahigh Rate Performance and High Energy Density. *Chemelectrochem.* **2017**, *4*, 369–375. [[CrossRef](#)]
49. Xu, K.B.; Li, W.Y.; Liu, Q.; Li, B.; Liu, X.J.; An, L.; Chen, Z.Q.; Zou, R.J.; Hu, J.Q. Hierarchical mesoporous NiCoO@MnO core-shell nanowire arrays on nickel foam for aqueous asymmetric supercapacitors. *J. Mater. Chem. A* **2014**, *2*, 4795–4802. [[CrossRef](#)]
50. Zhang, J.L.; Zhang, W.F.; Han, M.F.; Pang, J.; Xiang, Y.; Cao, G.P.; Yang, Y.S. Synthesis of nitrogen-doped polymeric resin-derived porous carbon for high performance supercapacitors. *Micropor. Mesopor. Mater.* **2018**, *270*, 204–210. [[CrossRef](#)]

51. Xu, J.; Li, J.Q.; Yang, Q.L.; Xiong, Y.; Chen, C.G. In-situ Synthesis of MnO₂@Graphdiyne Oxides Nanocomposite with Enhanced Performance of Supercapacitors. *Electrochim. Acta* **2017**, *251*, 672–680. [[CrossRef](#)]
52. Zhang, D.Y.; Zhang, Y.H.; Luo, Y.S.; Chu, P.K. Highly porous honeycomb manganese oxide@carbon fibers core-shell nanocables for flexible supercapacitors. *Nano Energy* **2015**, *13*, 47–57. [[CrossRef](#)]
53. Hao, J.N.; Liao, Y.Q.; Zhong, Y.Y.; Shu, D.; He, C.; Guo, S.T.; Huang, Y.L.; Zhong, J.; Hu, L.L. Three-dimensional graphene layers prepared by a gas-foaming method for supercapacitor applications. *Carbon* **2015**, *94*, 879–887. [[CrossRef](#)]

Sample Availability: Samples of the compounds are available from the authors.



© 2019 by the authors. Licensee MDPI, Basel, Switzerland. This article is an open access article distributed under the terms and conditions of the Creative Commons Attribution (CC BY) license (<http://creativecommons.org/licenses/by/4.0/>).